

AD-A269 451



2

ARMY RESEARCH LABORATORY



# Penetration of Tungsten Alloy Rods Into Shallow-Cavity Steel Targets

A. M. Rajendran and Patrick Woolsey

ARL-TR-216

August 1993

DTIC  
ELECTE  
SEP 17 1993  
S A D

93-21703



Approved for public release; distribution unlimited.

The findings in this report are not to be construed as an official Department of the Army position unless so designated by other authorized documents.

Citation of manufacturer's or trade names does not constitute an official endorsement or approval of the use thereof.

Destroy this report when it is no longer needed. Do not return it to the originator.

REPORT DOCUMENTATION PAGE			Form Approved OMB No. 0704-0188	
Public reporting burden for this collection of information is estimated to average 1 hour per response, including the time for reviewing instructions, searching existing data sources, gathering and maintaining the data needed, and completing and reviewing the collection of information. Send comments regarding this burden estimate or any other aspect of this collection of information, including suggestions for reducing this burden, to Washington Headquarters Services, Directorate for Information Operations and Reports, 1215 Jefferson Davis Highway, Suite 1204 Arlington, VA 22202-4302, and to the Office of Management and Budget, Paperwork Reduction Project (0704-0188), Washington, DC 20503.				
1. AGENCY USE ONLY (Leave blank)	2. REPORT DATE August 1993	3. REPORT TYPE AND DATES COVERED Final Report		
4. TITLE AND SUBTITLE  Penetration of Tungsten Alloy Rods Into Shallow-Cavity Steel Targets		5. FUNDING NUMBERS		
6. AUTHOR(S)  A. M. Rajendran and Patrick Woolsey				
7. PERFORMING ORGANIZATION NAME(S) AND ADDRESS(ES) U.S. Army Research Laboratory Watertown, Massachusetts 02172-0001 ATTN: AMSRL-MA-DA		8. PERFORMING ORGANIZATION REPORT NUMBER  ARL-TR-216		
9. SPONSORING/MONITORING AGENCY NAME(S) AND ADDRESS(ES) U.S. Army Research Laboratory 2800 Powder Mill Road Adelphi, Maryland 20783-1197		10. SPONSORING/MONITORING AGENCY REPORT NUMBER		
11. SUPPLEMENTARY NOTES				
12a. DISTRIBUTION/AVAILABILITY STATEMENT  Approved for public release, distribution unlimited			12b. DISTRIBUTION CODE	
13. ABSTRACT (Maximum 200 words)  This report presents a combined numerical and experimental study on penetration of tungsten heavy alloy long rods (L/D=10) into thick RHA steel plates. The main objective of this study was to establish the effects of a shallow cavity at the front surface of the steel plate on the depth of penetration (DOP). In the experiment, two target configurations were considered: one, a 127 mm flat thick plate, and the other, a 152 mm thick plate with a 25.4 mm deep and 19 mm diameter cavity. In both cases, the plate thickness was effectively 127 mm. Three experiments were performed at 1.5 km/sec on the shallow-cavity targets. These results were compared to existing penetration data obtained for flat plates over a velocity range of 1.1 to 1.7 km/sec. Based on the experimental results, the effect of the shallow cavity wall constraint on the penetration process was found to be insignificant. This experimental observation was predicted by numerical simulations before testing. Two different cavity diameters as well as the flat plate, were considered in the simulations. The code results matched the measured depths of penetration within the limits of experimental accuracy for all configurations examined. We also evaluated the effects of mesh and time step on the computational results.				
14. SUBJECT TERMS  Terminal ballistics, Modeling, Simulation, Penetration, Steel, Long rod penetrators			15. NUMBER OF PAGES 28	
			16. PRICE CODE	
17. SECURITY CLASSIFICATION OF REPORT Unclassified	18. SECURITY CLASSIFICATION OF THIS PAGE Unclassified	19. SECURITY CLASSIFICATION OF ABSTRACT Unclassified	20. LIMITATION OF ABSTRACT UL	

## Contents

	Page
Introduction . . . . .	1
Ballistic Testing Procedures . . . . .	2
Numerical simulations . . . . .	4
Material Strength . . . . .	6
Mesh Effect on the DOP . . . . .	8
Target Strength Effect on DOP . . . . .	10
Analysis of the Simulations . . . . .	11
Comparison with Data . . . . .	15
Summary and Conclusions . . . . .	16
Acknowledgments . . . . .	17
References . . . . .	17

## Figures

1.	Schematic of a shallow cavity target and a long rod penetrator . . . . .	2
2.	Penetration depth as a function of impact velocity for flat and shallow cavity targets . . . . .	4
3.	Fine mesh, flat target configuration . . . . .	5
4.	Schematic of the small shallow cavity target configuration . . . . .	5
5.	(a) Fine mesh for big cavity case and (b) Close-up mesh near the impact area at $t > 0$ . Dimensions are shown in meters . . . . .	7
6.	Comparison of DOP versus time between fine and coarse mesh for big cavity case . . . . .	9
7.	Comparison of the stress-strain curves between RHA and 4340 steel at strain rates of 0.001/s and 5000/s . . . . .	10
8.	Comparison of DOP versus time between the simulations using the RHA and 4340 steels . . . . .	10

9.	The effective plastic strain histories at the cavity edge location for the three target configurations . . . . .	11
10.	Comparison plot of elastic -plastic zone sizes between big cavity and flat target configurations . . . . .	12
11.	The definition of depth of penetration from the simulation results . . . . .	13
12.	Comparison plot of depth of penetration for the three target configurations . . . . .	14
13.	Comparison of depth of penetration between experimental data and EPIC simulations . . . . .	15

### Tables

1.	Penetrator dimensions, mass, and material . . . . .	3
2.	Test results . . . . .	3
3.	Mesh details and computing time . . . . .	6
4.	Johnson-Cook model constants . . . . .	8
5.	Computed depth of penetrations . . . . .	15

DATA QUANTITY INSPECTED 4

Accession For	
NTIS CRA&I	JED
DTIC TAB	
Unannounced	
Justification	
By	
Dist Name /	
Availability Codes	
Dist	Avail and/or Spec
A-1	

## Introduction

The applicability of hydrocode simulations to penetration problems is an issue of ongoing concern in the area of penetration mechanics and armor design. At present, there is a wide range of data available on the penetration of heavy alloy rods into thick targets having planar surfaces, and much effort has been put into modeling this case, with generally acceptable results. Information for other types of surfaces, however, is sparse. It is also of interest to determine the ability of currently available models to correctly track increasingly complex target configurations. These factors prompted the performance of a comparative study at the U.S. Army Research Laboratory's Materials Directorate, in which empirical investigation and hydrocode simulations were made of a target/penetrator system with a non-planar impact surface. The system employed was semi-infinite steel, with a tungsten heavy alloy long rod penetrator impacting at the bottom of a cylindrical cavity in the target.

At impact velocity levels below the hydrodynamic limit, the stresses imposed upon both penetrator and target materials are significantly greater than their yield strengths, but material strength still has a role in determining penetration behavior. The penetration of long rods under such conditions is a quasi-hydrodynamic process. Yielded penetrator material is basically ejected from the penetrator/target interface, in conjunction with failed target material. Many papers discussing this system are available; Tate [1] first performed an analysis of this system for a 1-dimensional case, while a thorough review and discussion of the models commonly employed for this type of penetration was made by Anderson et al [2]. A comprehensive collection of penetration data is available in the Penetration Mechanics Database report compiled by Anderson, Morris, and Littlefield [3].

The main objective of this report is twofold: first, to experimentally evaluate the effects of surface constraint on the penetration process of a tungsten heavy alloy (WHA) long rod into a thick RHA target, and second, to computationally predict the depth of penetration. For this purpose, two target configurations were considered. The first configuration is a flat 127 mm thick RHA plate, having a sufficiently large width to exclude the lateral boundary from affecting the penetration process. The second configuration is a 152 mm thick RHA plate with a 25.4 mm deep and 19 mm diameter shallow cavity. The projectile impacts at the bottom of this cavity, which is 25.4 mm from the free surface. The difference between the two configurations with respect to projectile penetration, is the presence of the cavity wall surrounding the impact plane close to the projectile in one case, against the absence of the cavity wall in the other case.

Prior to conducting the experiments, we performed a detailed numerical study to understand and predict the effect of penetration into a shallow cavity of a thick flat target. In the simulations, we employed the EPIC-2 Lagrangian finite element code [4]. The EPIC-2 (1986 version) code has been successfully installed on the Apollo series 400 and 700 workstations at

the Materials Directorate. For the present study, we found the workstation environment to be extremely useful and efficient. The results were analyzed using in-house post-processors [5].

In the "Ballistic Testing Procedures" section, the experiments on the two different targets are reported in detail, and the depth of penetration (DOP) values are tabulated. The "Numerical Simulation" section compares the hydrocode-predicted DOP with experimental measurements. In this section, the effects of target strength and mesh size on the penetration are also investigated.

### Ballistic Testing Procedures

The target employed was a monolithic plate of RHA (rolled homogeneous armor) steel (MIL-A- 12560, Class 3), with a total thickness of 152 mm (nominal 6 in.). A series of cylindrical holes with 19 mm (0.750 inch) diameter and 25.4 mm (1 inch) depth were cut into the plate with an end mill. These holes were spaced apart at a distance of 63.5 mm (2.5 inch) from center to center. The hole dimensions employed were chosen so as to minimize the cavity diameter while precluding the rod from contacting the cavity side wall during penetration, given a shot less than 3° total yaw. A schematic is shown in Figure 1 detailing the target geometry. The plate was held at 0° obliquity (i.e., normal to the line of flight). The average hardness of the plate was HRC 27. This corresponds to a quasi-static yield strength of approximately 0.9 GPa (125 ksi).

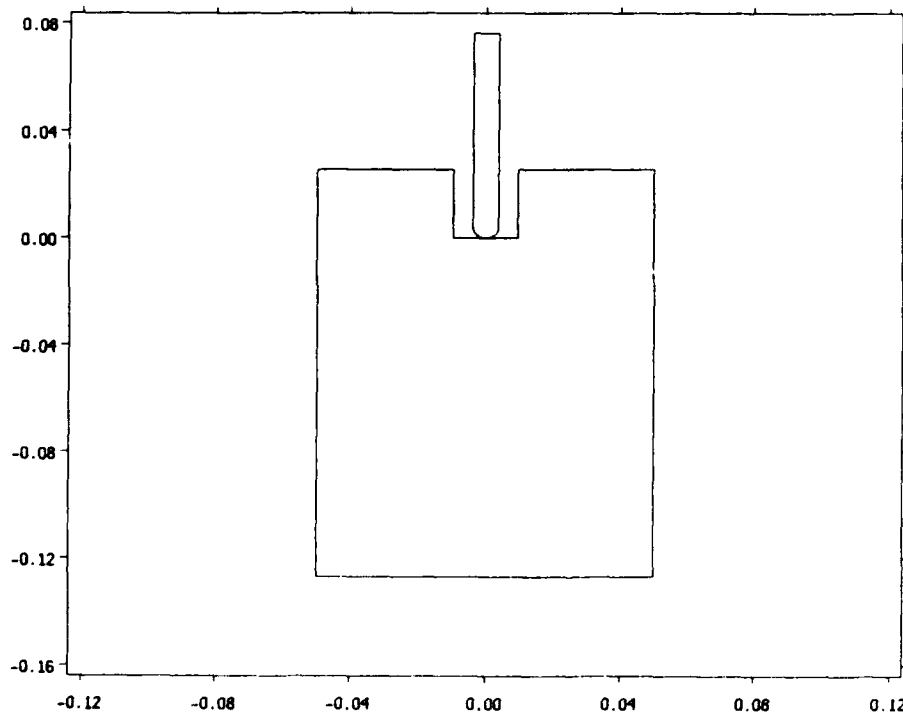


Figure 1. Schematic of a shallow cavity target and a long rod penetrator.

The penetrators were cylindrical rods with hemispherical noses, having aspect ratios (L/D) of 10:1, and average masses of 65.4 g. Dimensions are given in Table 1 below. The penetrator material is a 91% tungsten heavy alloy (WHA) material, designated X-27C.

**Table 1. Penetrator dimensions, mass, and material**

Length (mm)	Diameter (mm)	Mass (g)	Density (g/cm <sup>3</sup> )	Material
78.74	7.87	65.4	17.35'	WHA (X-27C)

Ballistic tests were conducted with a 20 mm smoothbore powder gun. The projectiles were launched in base-push sabot packages which employed a steel pusher disc. Projectile velocity and yaw were measured by means of an orthogonal flash X-ray system. A nominal striking velocity of 1500 m/s (4900 ft/s) was chosen to match that used in standard materials evaluation tests. The criterion for acceptance and inclusion of a test point was a total projectile yaw of less than 3°. However, the yaw was close to 3.4° in test #T61-92-3 as shown in Table 2.

**Table 2. Test results**

Test Number	Impact Velocity		Total Yaw (degrees)	DOP	
	m/s	ft/s		(mm)	(inch)
T61-92-1	1508	4948	0.78	73.7	2.90
T61-92-2	1501	4925	0.33	68.1	2.68
T61-92-3	1499	4919	3.40	67.0	2.64

The final depths of penetration into the RHA plate were obtained by direct measurement from cross sections, which were prepared by bandsaw cutting through the center of the penetration cavity. The reference penetration of the projectile into RHA steel of an equivalent hardness level had been previously determined [3]. At the nominal velocity, the reference penetration is 68.6 mm (2.70 inch) with a scatter of  $\pm 3.8\%$  (within two standard deviations). Penetration for the reference case (planar surface) is plotted as a function of velocity in Figure 2, together with the above results from the cylindrical cavity tests. The experimental results indicated that the effect of a shallow cavity at the front surface of the target did not influence the penetration mechanism. Within the limits of experimental error, the average values of DOP from the three shallow-cavity tests agreed with the DOP data from the flat plate targets.



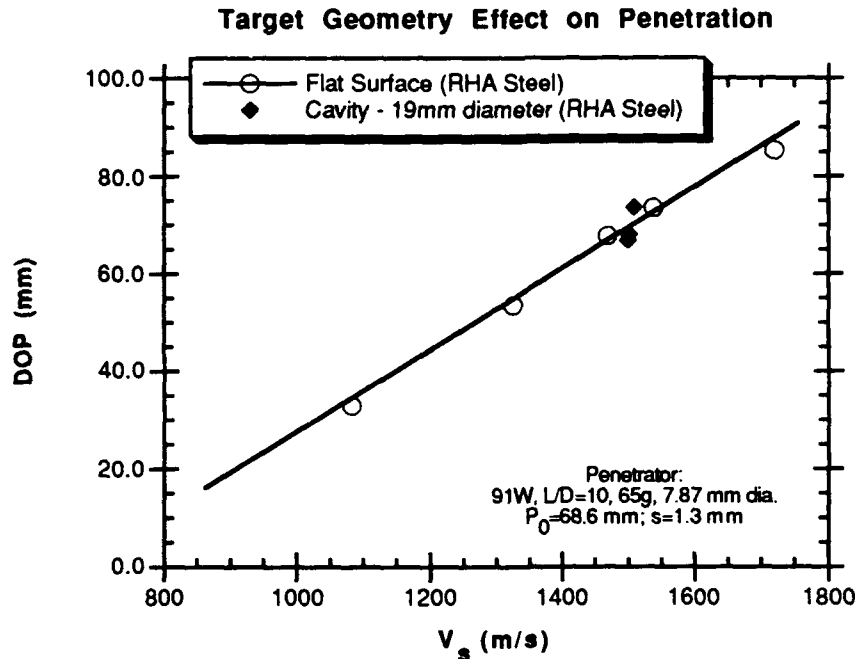


Figure 2. Penetration depth as a function of impact velocity for flat and shallow-cavity targets.

### Numerical Simulations

The main objective of the numerical simulations was to predict the depth of penetration (DOP) of the WHA long rod projectile into the RHA steel target and to compare these predictions with the measured DOP values. The 1986 version of the EPIC-2 finite element code [4] was employed in the numerical simulations. We employed the crossed-triangles option to discretize the target and penetrator. The material behavior was described using a strain rate, temperature, and pressure dependent strength model.

Three target configurations were considered: 1) a flat plate (target) of 127 mm thickness and 100 mm diameter, 2) a 152 mm thick plate with a shallow cavity of 19 mm diameter and 25.4 mm depth, and 3) a 152 mm thick plate with a shallow cavity of 11.54 mm diameter and 25.4 mm depth.

For convenience, we address the first configuration as "**flat target**", the second as "**big cavity**", and the third as "**small cavity**". The schematic plot of the big cavity target was shown earlier in Figure 1. The flat and small cavity target configurations are shown in Figures 3 and 4. The small cavity target was selected to provide a limiting case for confinement, which would be difficult to perform experimentally.

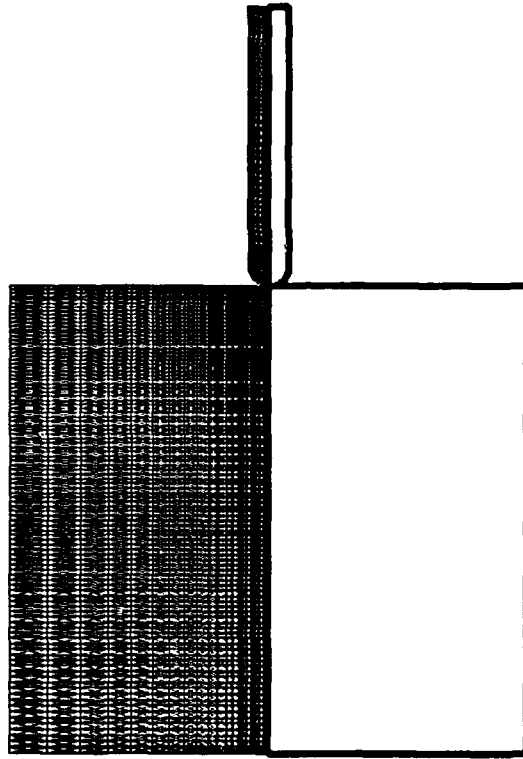


Figure 3. A fine mesh, flat target configuration.

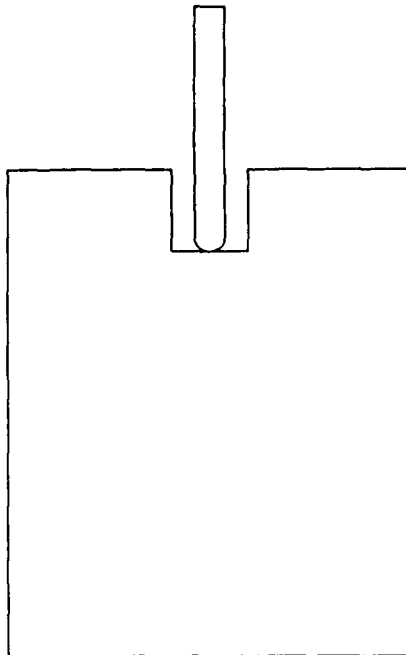


Figure 4. Schematic of the small shallow cavity target configuration.

In the initial simulations, a relatively coarse mesh was considered, but in later runs, finer meshes were used for the target. The projectile was described through elements of four columns and twenty rows. The aspect ratio of the elements near the impact regions was about one. In all meshes used, the aspect ratio of the elements was uniformly increased when moving towards the projectile tail. The cross triangle option in the EPIC code was used.

To study the effects of finite element mesh sizing on the calculated penetration depths, a fine mesh for the target was also employed. However, the projectile mesh was the same for both fine and coarse mesh target cases. For the flat target and big cavity cases, two different meshes were considered. For all cases, the finer mesh contained more than double the elements of the coarse mesh. Figure 5 shows an overall view as well as the close-up views at the impact region. The aspect ratio of the crossed triangle cells was again close to one.

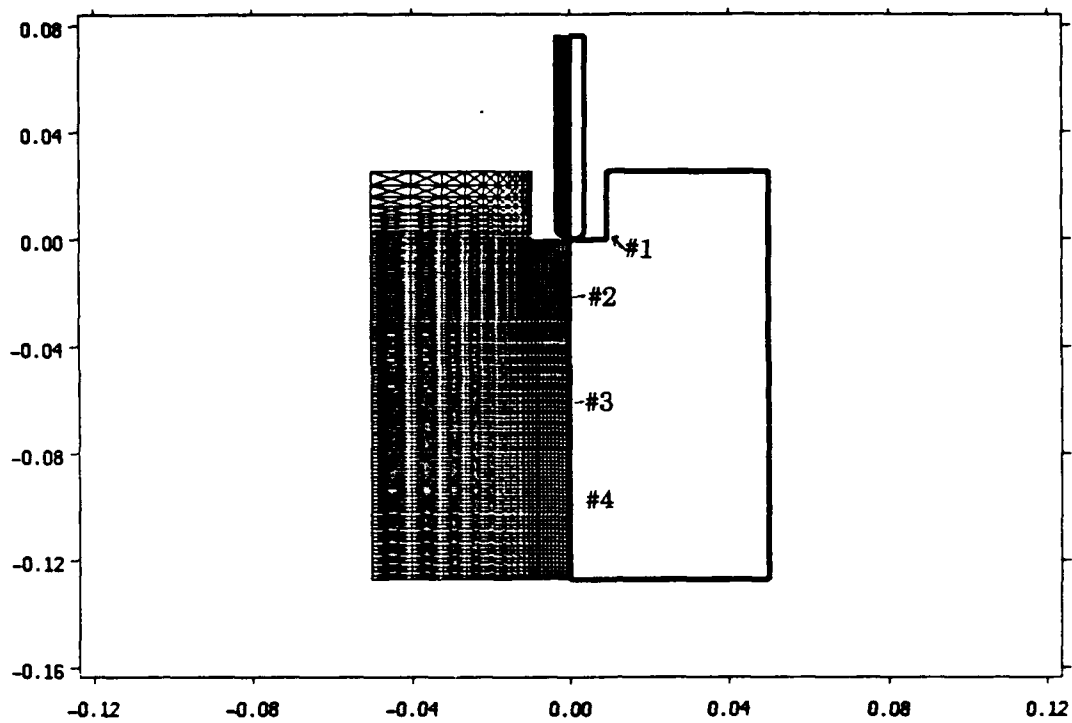
The EPIC-2 simulations runs were performed on the 700 series of Apollo workstations. The mesh details and computing times are both reported in Table 3. The finer meshes required about three to four times as long to solve as the coarser meshes.

**Table 3. Mesh details and computing time**

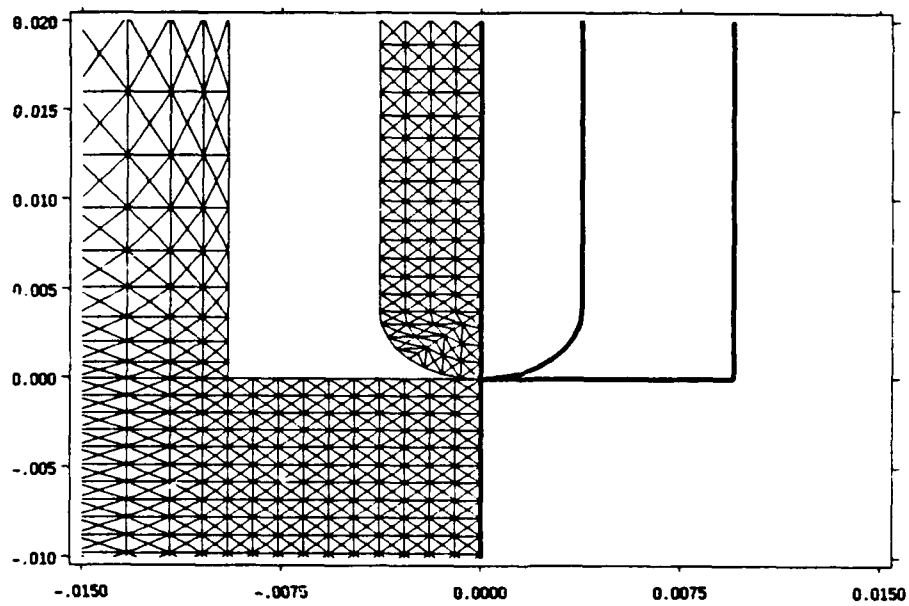
	Coarse Mesh						Fine Mesh			
Number of #	Flat		Big Cavity		Small Cavity		Flat		Big Cavity	
	Proj.	Target	Proj.	Target	Proj.	Target	Proj.	Target	Proj.	Target
Node	401	1661	401	1871	401	1951	401	4121	401	4331
Element	704	3200	704	3600	704	3760	704	8000	704	8400
Time (hrs)	1.03		1.14		1.40		2.98		4.05	

### Material Strength

The Johnson-Cook (J-C) strength model [6] was used to describe the high strain rate behavior of the WHA penetrator, and the RHA steel target. The J-C model constants for WHA were used from the EPIC material library. However, the RHA constants were based on the recent report of Gray III, et al [7]. In their model constants determination scheme, the compressive Hopkinson bar data at strain rates of 3000/sec to 7000/sec were employed. The J-C model is described by the following equation:



(a)



(b)

Figure 5. (a) Fine mesh for big cavity case and (b) close-up mesh near the impact area at  $t > 0$ . Dimensions are shown in meters.

$$Y = (A + B\epsilon^n)(1 + C \ln \dot{\epsilon}^*) (1 - T^{*m}) \quad (1)$$

where, A, B, C, n, and m are model constants, and  $T^*$  is given by,

$$\text{WHA: } T^* = \frac{(T - T_{\text{room}})}{(T_{\text{melt}} - T_{\text{room}})} \quad (2)$$

$$\text{Steel: } T^* = \frac{T}{T_{\text{melt}}} \quad (3)$$

with T is in degrees Kelvin. The subscript 'melt' and 'room' represent melting and room temperatures respectively. The WHA density was 17.35 g/cm<sup>3</sup> and RHA was 7.8 g/cm<sup>3</sup>. The bulk and shear moduli for the steel were 164 GPa and 77.5 GPa, respectively, and for WHA, 302 GPa and 124 GPa, respectively.

**Table 4. Johnson-Cook model constants**

Material	A (GPa)	B (GPa)	C	n	m
WHA	1.5	0.18	.016	.12	1.0
RHA steel	1.4	1.8	.005	.768	1.17

In the simulation, material failure is assumed to be due to erosion only. When the effective plastic strain in an element reached a value of 1.5, the material is eroded away in the calculation. The Mie-Gruneisen model, which describes the equation-of-state (EOS) of the material, was used to model WHA and RHA steel. The EOS parameters are available in the EPIC-2 library.

#### **Mesh Effect on the DOP**

Two calculations were performed using a coarse mesh and a fine mesh for the target to examine the effect of mesh on the computational results. The fine mesh had more than twice the number of nodes and elements compared to the coarse mesh. The target elements inside a radius of 9.5 mm were uniformly small with an aspect ratio of about 1. This radius of 9.5 mm was

divided with an uniform spacing of 0.95 mm. The element size was geometrically increased along the radius direction beyond the radius of 9.5 mm, while the size of the element along the penetration direction (z-direction) remained at 0.95 mm. The main difference between the two meshes was in the coarseness of the elements along the z-direction. In the fine mesh, this size was kept constant in the entire target thickness; however, in the coarse mesh, the element size along z was geometrically increased. The DOP results for the fine mesh and the coarse mesh are shown in Figure 6. The DOP values compared very well for about 100 microseconds, while later the values started slightly differing. The calculated DOP between the two meshes differed by about 5 mm. This difference amounts to a scatter of 5.5 percent in the DOP values. In general, both meshes used would be expected to give dependable results due to the relatively small element sizes employed. However, increasing the number of elements in the finer mesh did improve the predicted value of DOP as compared to the coarser mesh. In Figure 6, the DOP drops slightly beyond 150  $\mu$ s due to rebounding of the residual penetrator.

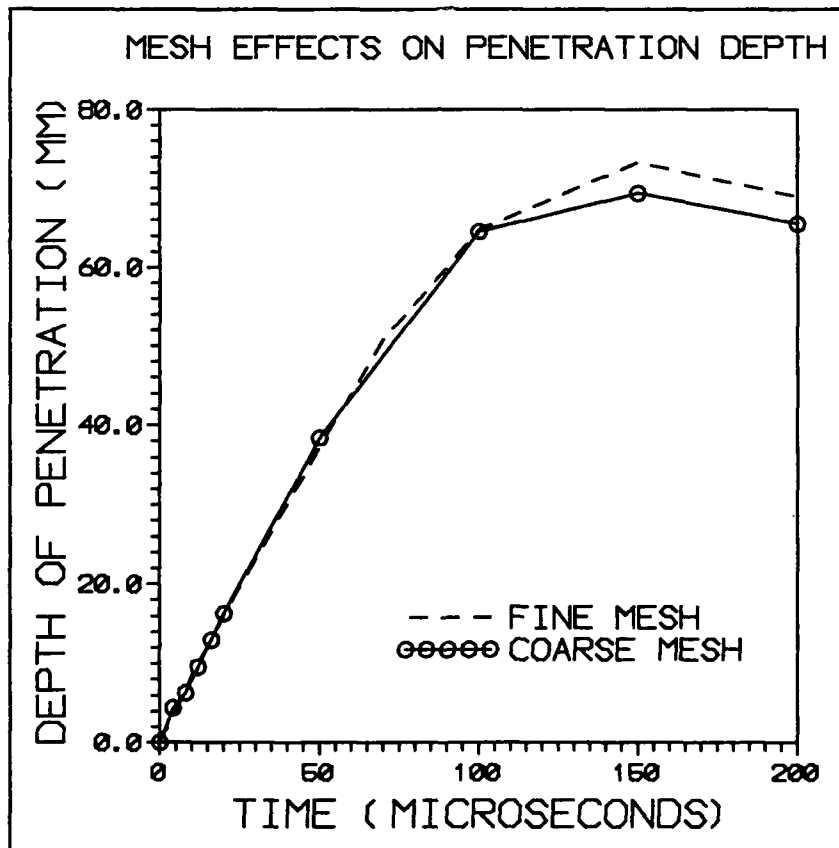


Figure 6. Comparison of DOP versus time between fine and coarse mesh for big cavity case.

## Target Strength Effect on DOP

The effect of target material strength on the DOP was examined through two simulations, both using the fine mesh configuration. In the first simulation, the material is realistically described using the high strain rate dynamic compressive data obtained from RHA steel. In the second simulation, the stress-strain curves generated by the EPIC-2 library for a relatively soft 4340 steel were employed.

The stress-strain curves generated using the J-C model for RHA and 4340 steels at quasi-static and dynamic strain rates are shown in Figure 7. The DOP in low strength 4340 steel was about 20% higher than the DOP in high strength RHA. It is fairly well known that the penetration in thick targets, where the failure process is mainly due to erosion, is sensitive to the stress-strain response (strength) of the target material. The present numerical modeling demonstrated the expected effects of strength on DOP. In Figure 8, the DOP values obtained using the two different strengths are compared. These results were obtained for the big cavity target. Similar results were obtained for the flat targets.

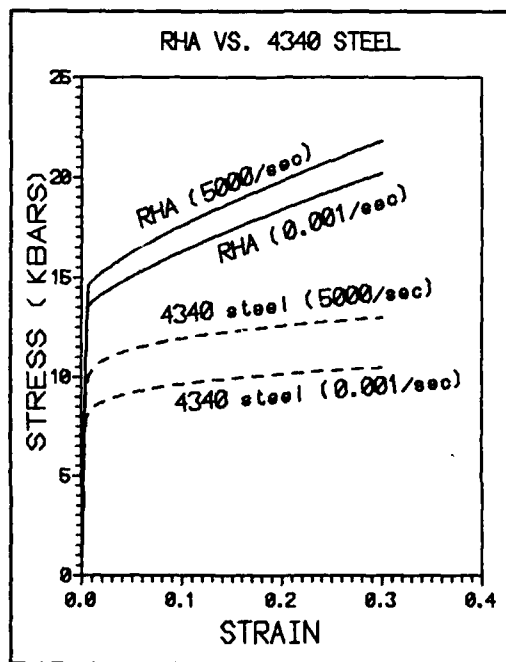


Figure 7. Comparison of the stress-strain curves between RHA and 4340 steel at strain rates of 0.001/s and 5000/s.

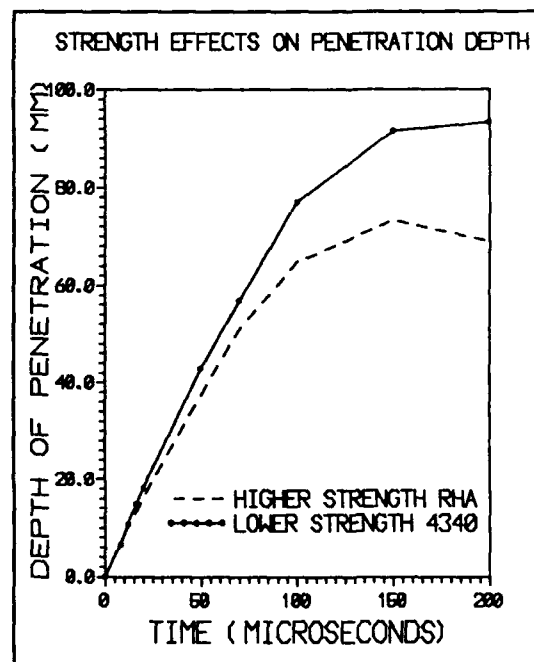


Figure 8. Comparison of DOP versus time between the simulations using the RHA and 4340 steels.

## Analysis of the Simulations

In this section, the computational results from the three simulations of the flat plate, the big shallow cavity, and the small shallow cavity configurations, are analyzed in details. For this purpose, we considered the effective plastic strain histories of four elements at various locations of the target (see Figure 5). For simplicity, these elements will be referred to as element #1, element #2, element #3, and element #4. The actual element numbers in the simulations are different. The first element is located at a radial distance which corresponds to the edge of the large shallow cavity at the top face of the target. The other three elements are located at depths of 30, 60, and 90 mm below the impact plane along the axis of symmetry. The effective plastic strain  $\epsilon_{eff}^p$  of element #1 as a function of time is compared for the three cases in Figure 9. Rapid plastic strain accumulation occurs in all cases; however, accumulation to the erosion strain level (1.5) occurs sooner in the big cavity, followed by the small cavity, and flat target. The plastic flow occurs rapidly due to stress concentration at the cavity edge. This is also true in the case of the small cavity; however, the effect of cavity edge is less pronounced due to the presence of large plastic flow generated by the projectile near the impact region. This region is closer to the cavity edge in the small cavity case.

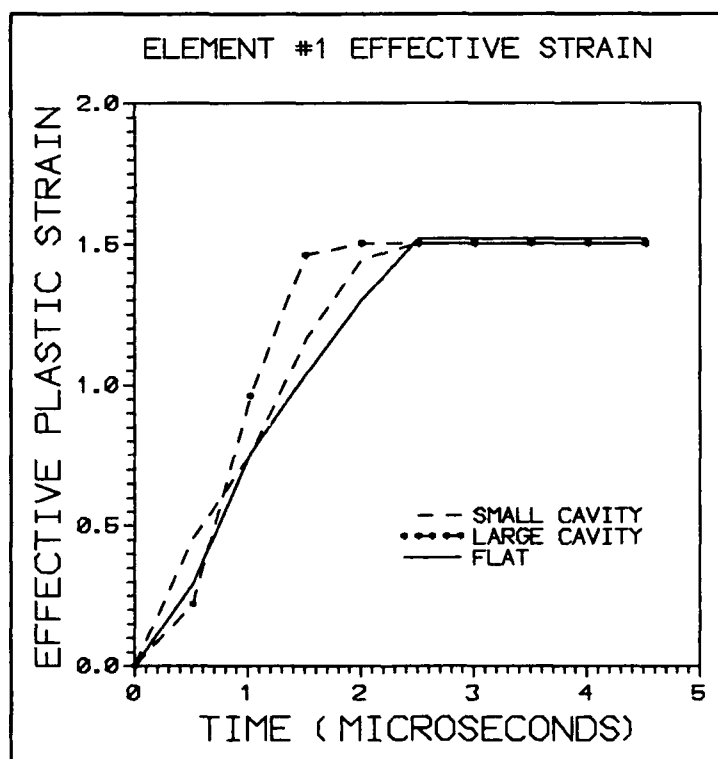


Figure 9. Effective plastic strain histories at the cavity edge location for the three target configurations.



In the big cavity case, the cavity edge is sufficiently far away from the projectile generated plastic flow regions that the plastic zone near the edge initially does not interfere with the plastic flow region at the impact area. In fact, the present study was initiated to find whether the plastic flow near the side wall of the shallow cavity would eventually influence and change the depth of penetration. At the impact velocity selected, this effect is short lived only lasting for about one microsecond. The effective plastic strain values reach the erosion strain level of 1.5 and the code erodes the element away. Similar results were observed for the other elements along the axis of symmetry. Though the cavity edge was not anywhere near these elements, the plastic strain in elements of the big cavity configuration accumulated faster than the plastic strain in the small and flat cases.

To compare the elastic-plastic regions of the big cavity (solid line) and flat (dashed line) targets, the  $\epsilon_{eff}^p$  contours for a value of 0.01 are plotted in Figure 10. The elastic-plastic zones are very similar, except around the cavity edge. In the big cavity case, the plastic zone is slightly larger than it is in the flat target case. However, this slight difference did not influence the DOP. The plastic strain contour in the big cavity case is tied around the cavity, whereas in the flat target case it spreads away from the impact plane.

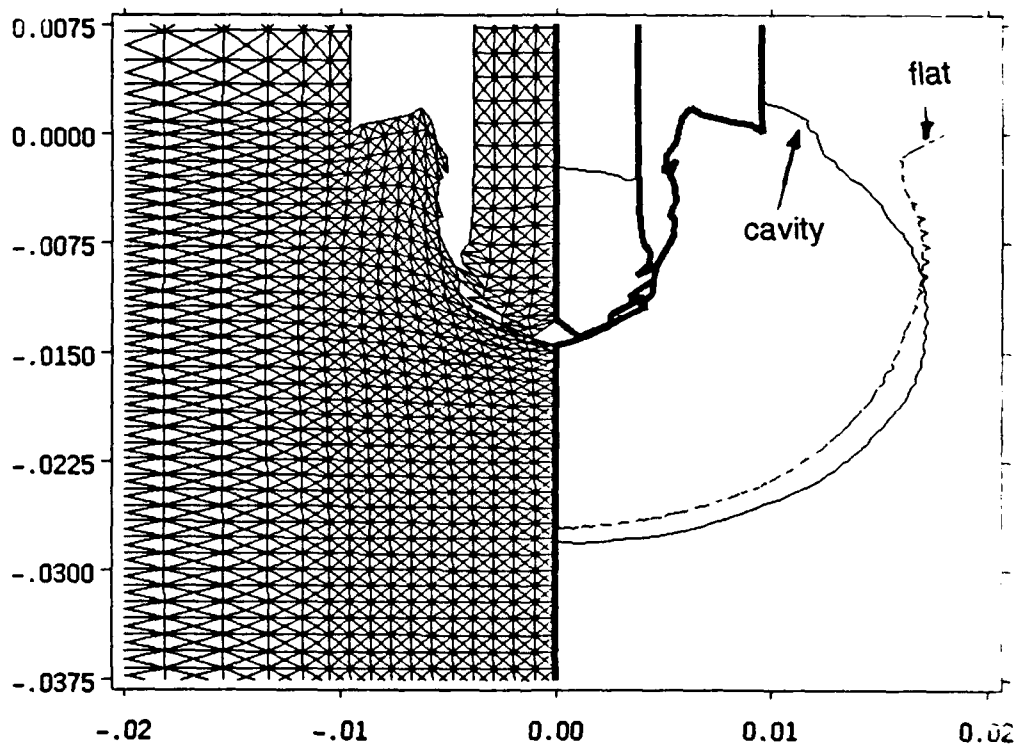


Figure 10. Comparison plot of elastic-plastic zone sizes between big cavity and flat target configurations.

To further validate the analysis, the penetration depth was estimated from the EPIC-2 results, using a calculation based on the position of the leading face of the projectile, as shown in Figure 11. The EPIC-2 results obtained for erosion strains values of 1.5 and above were almost identical. The effective plastic strain based failure model was not used in the calculations. The failure of the material elements were entirely due to erosion. In the simulation, the leading face of the deformed projectile was not planar due to erosion. Therefore, the leading node at the axis-of-symmetry was used in the DOP estimation from the deformed mesh of the projectile-target configuration.

The secondary penetration directly beneath the projectile was not considered as part of the penetration depth in the analysis. This secondary penetration could be due to numerical artifacts. The experimental measurements did not exhibit any such secondary penetration. The measured DOP is also based on the distance between the impact plane and the leading edge of the residual penetrator. Therefore, the definition of the depth of penetration is consistent with the experimental measurements.

A special purpose post-processor [5] was used to obtain the location (Z-coordinate) of the uneroded leading point on the projectile from the EPIC-2 output file which stored the deformed projectile-target configurations at various time intervals.

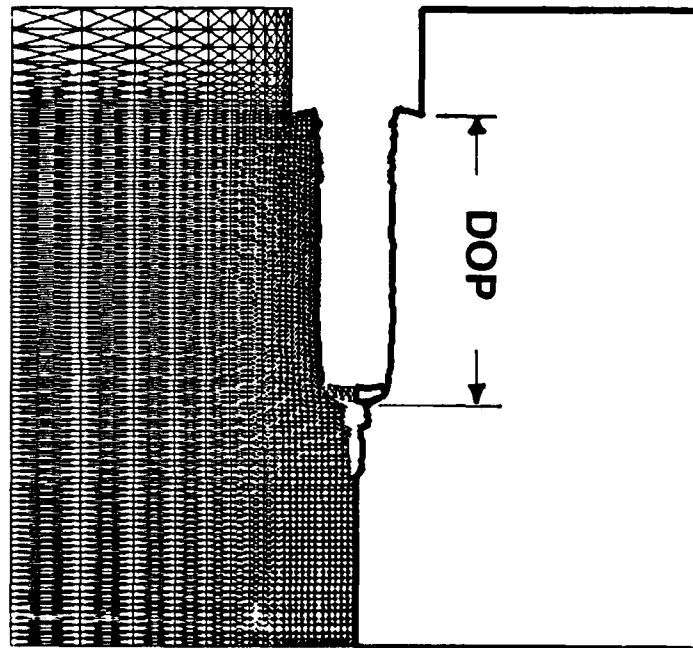


Figure 11. The definition of depth of penetration from the simulation results.

In Figure 12, the penetration depths as function of time are plotted for the three cases. It must be noted that while a fine mesh was used for the flat target and big cavity, only a coarse mesh was used for the small cavity. The slight difference observed between the small cavity and the other two cases is therefore assumed to result from the mesh effect. It was shown earlier (see Figure 6) that the coarse mesh under-predicted the DOP, in general. Therefore, according to these simulations and ignoring the mesh effects, the DOP of a WHA long rod projectile into a thick RHA target is not influenced by the constraint conditions imposed by the shallow cavity. Computed DOP values from the EPIC simulations for the 1500 m/s (4900 ft/s) impact condition are tabulated in Table 5.

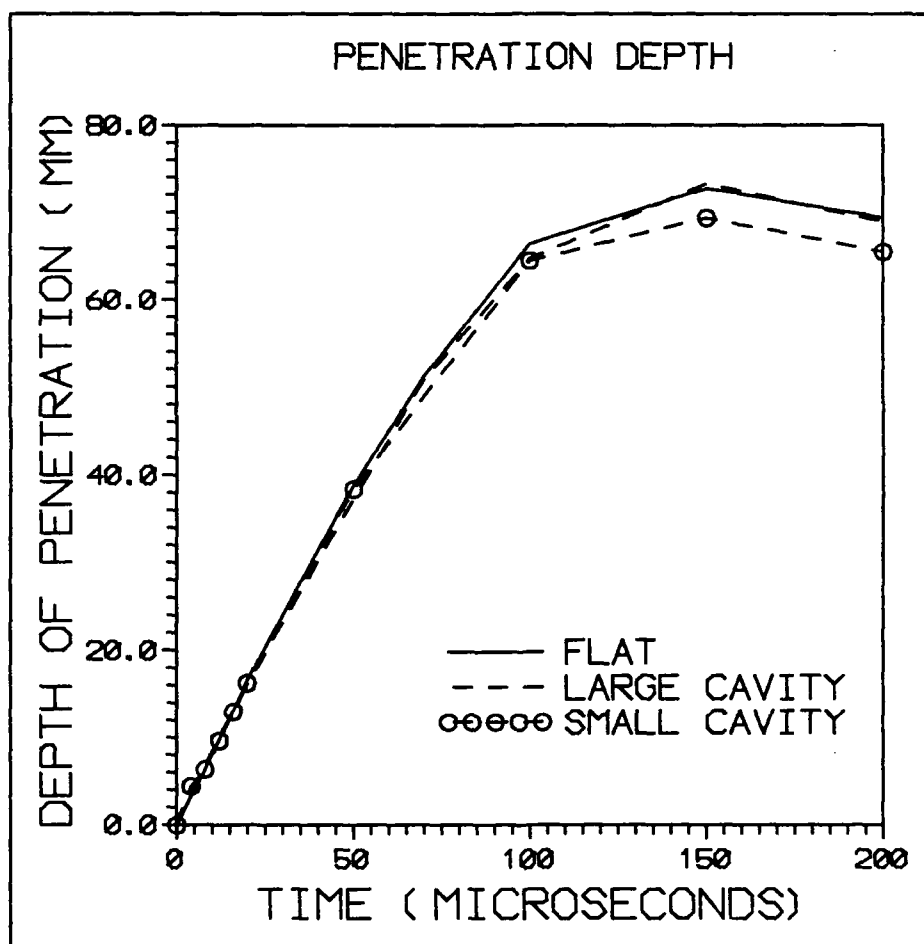


Figure 12. Comparison plot of DOP for the three target configurations.

**Table 5. Computed depth of penetrations**

Case	DOP (mm)
Flat Fine Mesh	72.7
Flat Coarse Mesh	71.7
Big Cavity Fine Mesh	73.3
Big Cavity Coarse Mesh	69.8
Small Cavity Coarse Mesh	67.6

### Comparison with Data

In comparing the measured data from the penetration experiments with the simulations, results from both the fine mesh and the coarse mesh simulations were considered. In Figure 13, the computed values are compared with the data. The predicted values matched extremely well with the experimental measurements, all falling within the limits of the variability in the empirical results.

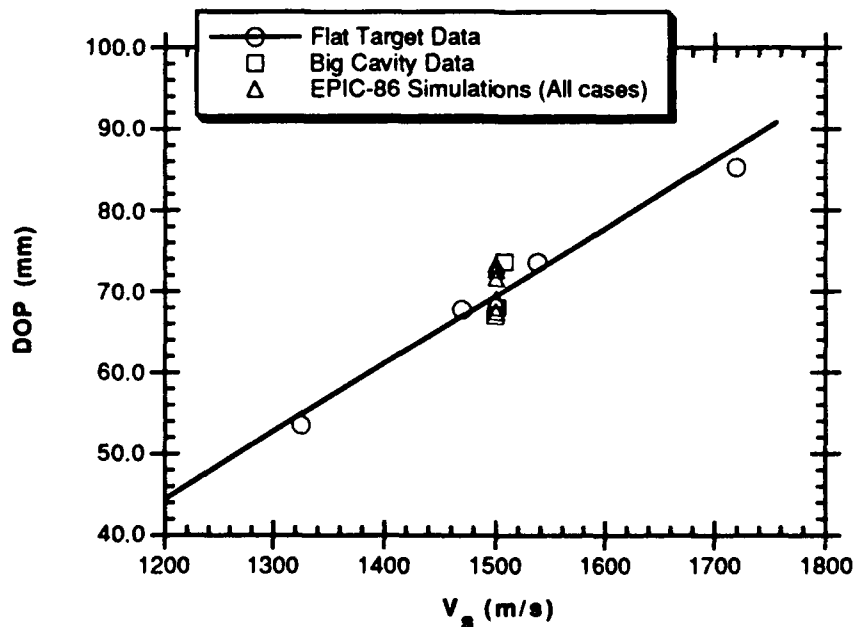


Figure 13. Comparison of DOP between experimental data and EPIC simulation.

## Summary and Conclusions

During the past decade, the hydrocode simulation capabilities have been steadily improving and hydrocodes have seen significant use as design tools in warhead and target analyses. Due to lack of documentation, many computational studies remain unnoticed or stay as unpublished works. This leads to a continual need to 'reinvent the wheel' when undertaking such studies. Therefore, we felt it necessary to document the outcome of our recently conducted combined experimental/computational study of WHA penetration into thick RHA steel through this report.

The main objective of the study was to investigate the effects of a shallow cavity at the front surface of a thick target on the depth of penetration of a long rod projectile. Prior to conducting the experiments, computational studies were performed using the EPIC-2 Lagrangian finite element code. The secondary objective was to demonstrate the applicability of code calculation in predicting the penetration of a metal long rod into a metal target. In the simulation, three target configurations were considered: 1) a 127 mm thick flat target, 2) a 152 mm thick flat target with a 9.5 mm radius and 25.4 mm deep shallow cavity at the front face, and 3) a 152 mm thick flat target with a 5.7 mm radius and 25.4 mm deep shallow cavity at the front.

The effects of mesh size and material strength on the computed DOP were initially examined. A relatively coarser mesh yielded results that were comparable to the results from a very fine mesh. In general, if the mesh is designed properly, we can successfully eliminate the need for excessive refinement of the mesh. It was possible to employ a fine mesh near the penetration region and a coarse mesh further away from this region. The aspect ratio of cells or elements near the penetration event should be close to one to ensure realistic results.

The accurate description of dynamic material behavior is also very important in the hydrocode simulation. The effect of target strength on the depth of penetration was demonstrated in this study. The calculated DOP using a softer material with an initial yield strength of 0.7 GPa at a strain rate of 5000/sec, was significantly higher than the calculated value for a stronger material (1.4 GPa). In the simulations, we accurately modeled the high strain rate behavior of RHA steel using the data from dynamic stress-strain curves. The Johnson-Cook strength model constants for RHA are available in the open literature.

The comparisons of time and contour plots of effective plastic strain between the three cases revealed that the effect of the cavity wall on the penetration process was negligible. Since the plastic flow regions at the penetration sites rapidly merged with the plastic strain region around the cavity edge, the penetration process proceeded as if there was no cavity. The cavity wall did not modify the surface boundary conditions so as to provide any additional resistance to the penetrator, a result which was counter to our initial expectation. The computed depth of

penetration values for the three cases were very similar. The computed values compared extremely well with the measured data. In summary, the computational results did provide an improved understanding of the penetration process in targets of this sort. The code also provided an accurate quantitative measure of penetration in the target.

### **Acknowledgments**

The authors gratefully acknowledge the support of Colin Freese in providing special purpose post-processors for the EPIC-2 code to analyze the results. The authors would like to thank Mr. W. Fred Cost for his technical contributions. They also appreciate the assistance of Messrs. John Segalla and John Loughlin in performing the ballistic testing, and George Dewing for sample preparation.

### **References**

1. Tate, A., "**A Theory for the Deceleration of Long Rods After Impact**," J. Mech. Phys. Solids 15, 387 (1967).
2. Anderson, Jr., C.E., and Walker, J.D., "**An Examination of Long Rod Penetration**," Int. J. of Impact Eng., 4, 481- 501 (1991).
3. Anderson, Jr., C.E., Morris, B.L., and Littlefield, D.L., "**A Penetration Mechanics Database**," SwRI Report 3593/001, (January 1992).
4. Johnson, G. R. and Stryk, R. A., "**User Instructions for the EPIC-2 Code**," AFATL-TR-86-51, Eglin Air Force Base, FL, (1986).
5. Colin Freese, Unpublished Works, Materials Directorate, ARL, Watertown, MA 02172
6. Johnson, G. R. and Cook, W. H., "**Fracture Characteristics of Three Metals Subjected to Various Strains, Strain Rates, Temperatures, and Pressures**," *Eng. Fracture Mechanics*, 21, 31-48, (1985).
7. Gray III, G.T., Chen, S.R., Wright, W., and Lopez, M.F., "Constitutive Equations for Annealed Metals Under Compression at High Strain Rates and High Temperatures," Los Alamos National Laboratory Report, Los Alamos, New Mexico 87545, 1993.

# DISTRIBUTION LIST

No. of Copies	To
1	Office of the Under Secretary of Defense for Research and Engineering, The Pentagon, Washington, DC 20301
	Director, U.S. Army Research Laboratory, 2800 Powder Mill Road, Adelphi, MD 20783-1197
1	ATTN: AMSRL-OP-CI-AD, Technical Publishing Branch
1	AMSRL-OP-CI-AD, Records Management Administrator
1	AMSRL-SS
	Commander, Defense Technical Information Center, Cameron Station, Building 5, 5010 Duke Street, Alexandria, VA 22304-6145
2	ATTN: DTIC-FDAC
1	MIA/CINDAS, Purdue University, 2595 Yeager Road, West Lafayette, IN 47905
	Commander, Army Research Office, P.O. Box 12211, Research Triangle Park, NC 27709-2211
1	ATTN: Information Processing Office
1	Andrew Crowson
1	Dr. Kailasam
	Commander, U.S. Army Materiel Command, 5001 Eisenhower Avenue, Alexandria, VA 22333
1	ATTN: AMCSCI
	Commander, U.S. Army Materiel Systems Analysis Activity, Aberdeen Proving Ground, MD 21005
1	ATTN: AMXSY-MP, H. Cohen
	Commander, U.S. Army Missile Command, Redstone Arsenal, AL 35809
1	ATTN: AMSMI-RD-CS-R/Doc
	Commander, U.S. Army Armament, Munitions and Chemical Command, Dover, NJ 07801
1	ATTN: Technical Library
	U.S. Army Communications and Electronics Command, Fort Monmouth, NJ 07703
1	ATTN: Technical Library
	Commander, U.S. Army Natick Research, Development and Engineering Center, Natick, MA 01760-5010
1	ATTN: Technical Library
	Commander, U.S. Army Satellite Communications Agency, Fort Monmouth, NJ 07703
1	ATTN: Technical Document Center
	Commander, U.S. Army Tank-Automotive Command, Warren, MI 48397-5000
1	ATTN: AMSTA-ZSK
1	AMSTA-TSL, Technical Library
1	AMSTA-RSK, Samuel Goodman
	Commander, White Sands Missile Range, NM 88002
1	ATTN: STEWS-WS-VT

No. of Copies	To
1	President, Airborne, Electronics and Special Warfare Board, Fort Bragg, NC 28307 ATTN: Library
1	Director, U.S. Army Research Laboratory, Aberdeen Proving Ground, MD 21005-5066 ATTN: AMSRL-WT
1	AMSRL-WT-TA, George Hauver
1	AMSRL-WT-TD, Michael J. Scheidler
1	AMSRL-WT-TC, Kent Kinsey
1	AMSRL-WT-TD, Thomas W. Wright
1	AMSRL-WT-TD, Glenn Randers-Pehrson
1	AMSRL-WT-TD, Steven Segletes
1	AMSRL-TB-W
1	AMSRL-TB-AM
1	AMSRL-TB-P
1	AMSRL-AMB-TBD
1	William Gooch
1	Commander, Dugway Proving Ground, UT 84022 ATTN: Technical Library, Technical Information Division
1	Air Force Materials Directorate, WPAFB, OH 45433 ATTN: Dr. Theodore Nicholas
1	NASA - Langley Research Center, Hampton, VA 23665-5225
1	U.S. Army Vehicle Propulsion Directorate, NASA Lewis Research Center, 2100 Brookpark Road, Cleveland, OH 44135-3191 ATTN: AMSRL-VP
1	Director, Defense Intelligence Agency, Washington, DC 20340-6053 ATTN: ODT-SA (Mr. Frank Jaeger)
1	Air Force Armament Laboratory, Eglin Air Force Base, FL 32542-5434 ATTN: J. C. Foster, Jr.
1	W. H. Cook
1	Naval Post Graduate School, Monterey, CA 93943 ATTN: Joseph Sternberg, Code EW
1	Lawrence Livermore, National Laboratory, Livermore, CA 94550 ATTN: J. E. Reaugh, L-290
1	R. L. Landingham, MC L-369
1	Dr. M. Finger, L-38
1	Daniel J. Steinberg
1	Carl R. Cline
1	Naval Surface Warfare Center, Silver Spring, MD 20903-5000 ATTN: F. J. Zerilli, Code R13
1	R. H. Garrett, Jr.
1	Naval Surface Warfare Center, Dahlgren, VA 22448 ATTN: William H. Holt, Naval Code G35



No. of Copies	To
	Los Alamos National Laboratory, Los Alamos, NM 87545
1	ATTN: Mike Burkett
1	J. Repa, DRA-CDT, MS F668
1	J. W. Straight, M-8, MS J960
1	R. Karpp, M-8, J960
1	J. Taylor, ADDRA, MS A110
1	Dr. P. S. Follansbee, MST-5, MS G730
1	Dr. J. N. Johnson, T-14, MS B214
1	Dr. P. J. Mauldin, N-6, MS K557
1	Dr. F. Adessio, T-3, MS B216
1	Thomas F. Adams, X-3, MS F663
1	G. E. Cort, ATAC, MS K574
1	Denise Hunter
1	Dave Mandell
1	Samuel R. Skaggs
1	Anna Zurek
1	Dr. B. M. Hogan
	Southwest Research Institute, 6220 Culebra Road, San Antonio, TX 78238
1	ATTN: James Lankford
1	Dr. C. E. Anderson
1	David Littlefield
	Southwest Research International, 333 Ravenswood Avenue, Menlo Park, CA 94025
1	ATTN: Richard Klopp
	Institute for Defense Analysis, 1801 N. Beauregard Street, Alexandria, VA 22311-1772
1	ATTN: Dr. George Mayer
1	Dr. Marc A. Adams, JPL MS 97-B, 4800 Oak Grove Drive, Pasadena, CA 91109
1	P.D. Buckley, NMIMT, TERA Group, Socorro, NM 87801
	California Institute of Technology, Geophysics Division MS/252-21, Pasadena, CA 91125
1	ATTN: Professor T. J. Ahrens
	Director, Benet Weapons Laboratory, LCWSL, USA AMCCOM, Watervliet, NY 12189
1	ATTN: AMSMC-LCB-TL
1	AMSMC-LCB-R
1	AMSMC-LCB-RM
1	AMSMC-LCB-RP
	Commander, U.S. Army Foreign Science and Technology Center, 220 7th Street, N. E., Charlottesville, VA 22901-5396
3	ATTN: AIFRTC, Applied Technologies Branch, Gerald Schlesinger
	Commander, U.S. Army Aeromedical Research Unit, P.O. Box 577, Fort Rucker, AL 36360
1	ATTN: Technical Library
	U.S. Army Aviation Training Library, Fort Rucker, AL 36360
1	ATTN: Building 5906-5907

No. of Copies	To
1	Commander, U.S. Army Agency for Aviation Safety, Fort Rucker, AL 36362 ATTN: Technical Library
1	Commander, Clarke Engineer School Library, 3202 Nebraska Ave., N, Fort Leonard Wood, MO 65473-5000 ATTN: Library
1	Commander, U.S. Army Engineer Waterways Experiment Station, P.O. Box 631, Vicksburg, MS 39180 ATTN: Research Center Library
1	Commandant, U.S. Army Quartermaster School, Fort Lee, VA 23801 ATTN: Quartermaster School Library
1	Naval Research Laboratory, Washington, DC 20375 ATTN: Dr. G. R. Yoder - Code 6384
1	Chief of Naval Research, Arlington, VA 22217 ATTN: Code 471
1	Commander, U.S. Air Force Wright Research & Development Center, Wright-Patterson Air Force Base, OH 45433-6523 ATTN: WRDC/MLLP, M. Forney, Jr. WRDC/MLBC, Mr. Stanley Schulman
1	NASA - Marshall Space Flight Center, MSFC, AL 35812 ATTN: Mr. Paul Schuerer/EH01
1	U.S. Department of Commerce, National Institute of Standards and Technology, Gaithersburg, MD 20899 ATTN: Stephen M. Hsu, Chief, Ceramics Division, Institute for Materials Science and Engineering
1	Committee on Marine Structures, Marine Board, National Research Council, 2101 Constitution Avenue, N. W., Washington, DC 20418
1	Materials Sciences Corporation, Suite 250, 500 Office Center Drive, Fort Washington, PA 19034
1	Charles Stark Draper Laboratory, 555 Technology Square, Cambridge, MA 02139
1	Wyman-Gordan Company, Worcester, MA 01601 ATTN: Technical Library
1	General Dynamics, Convair Aerospace Division, P.O. Box 748, Fort Worth, TX 76101 ATTN: Mfg. Engineering Technical Library
1	Plastics Technical Evaluation Center, PLASTEC, ARDEC, Bldg. 355N, Picatinny Arsenal, NJ 07806-5000 ATTN: Harry Pebly

No. of Copies	To
1	Department of the Army, Aerostructures Directorate, MS-266, U.S. Army Aviation R&T Activity - AVSCOM, Langley Research Center, Hampton, VA 23665-5225
1	Department of the Army, Armament Research and Development Center, Dover, NJ 07801 ATTN: Dr. E. Bloore
1	GTE Products Corporation, Towanda, PA 18848 ATTN: Jeff Gonzalez
1	RARDE, Fort Halstead - Sevenoaks, TN14 7BP Kent, England ATTN: Dr. Phillip Church
1	Department of FV&S7, DRA (Chertsey), Chobham Lane, Chertsey, Surrey, England ATTN: Dr. Anthony Hawkins
1	National Defense Research Establishment, Box 27322, S-102 54 Stockholm, Sweden ATTN: Dr. Per-Olof Olsson
1	Brown University, Division of Engineering, 182 Hope Street, Providence, RI 02912 ATTN: Ben Freund
1	California Research & Technology, Inc., 5117 Johnson Drive, Pleasanton, CA 94566 ATTN: Dennis L. Orphal
1	The Carborundum Company, P.O. Box 1054, Niagra Falls, NY 19302 ATTN: Robert Palia
1	Alme and Associates, 9650 Santiago Road, STE 102, Columbia, MD 21045 ATTN: Marvin L. Alme
1	Institute for Advanced Technology, 4030-2 West Braker, Austin, TX 78759-5329 ATTN: Stephen Bless
1	University of Dayton Research Institute, KLA14, 300 College Park, Dayton, OH 45469-0182 ATTN: N. Singh Brar
1	University of Dayton, Building JPC 201, Dayton, OH 45469 ATTN: Mr. David J. Grove
1	General Dynamics, Land Systems Division, P.O. Box 1800, Warren, MI 48090 ATTN: Wayne A. Burke
1	General Research Corporation, 5383 Hollister Avenue, Santa Barbara, CA 93160-6770 ATTN: Alex Charters
1	T. L. Menna
1	Sandia National Laboratories, P.O. Box 5800, Albuquerque, NM 87185 ATTN: Peter Chen
1	Dr. Dennis E. Grady, ORG 1533
1	Jack L. Wise

No. of Copies	To
1	The Pentagon, ODDR&E, Washington, DC 20305 ATTN: W. E. Snowden
1	DARPA/Materials Science Office, 1400 Wilson Boulevard, Arlington, VA 22209-2308 ATTN: B. Wilcox
1	Trans Science Corporation, P.O. Box 2727, La Jolla, CA 92038 ATTN: G. A. Hegemier
1	The University of Texas at Austin, Austin, TX 78712 ATTN: Eric Farenthold, Department of Mechanical Engineering
1	Michael Marder, Department of Physics, RLM 14.212
1	Steve Gross, Center for Non-Linear Dynamics, RLM 14
1	Ching-Hsie Yew, Aerospace Engineering Department, WRW 316B
1	Ahmed Shaaban, Aerospace Engineering Department, WRW 316B
1	Chadee Persad, Institute for Advanced Technology
1	Purdue University, School of Aeronautics & Astronautics, West Lafayette, IN 47907 ATTN: Horacio D. Espinosa
1	University of California - San Diego, Department of Applied Mechanics & Engineering Services - R011, La Jolla, CA 92093-0411 ATTN: Sia Nemat-Nasser
1	DARPA/TTO, 3701 North Fairfax Drive, Arlington, VA 22203-1714 ATTN: Robert Kocher
1	Lanxide Armor Products, Inc., 1300 Marrows Road, P.O. Box 6077, Newark, DE 19714-6077 ATTN: Katherine T. Leighton
1	University of Hawaii at Monoa, Mineral Physics Group, Department of Geology & Geophysics 255 Correa Road, Honolulu, HI 96822 ATTN: Murli Manghnani
1	Michigan Technical University, Department of Mechanical Engineering, 1400 Townsend Drive, Houghton, MI 49931-1295 ATTN: Bill Predebon
1	Kaman Sciences Corporation, P.O. Box 7463, 1500 Garden of the Gods Road, Colorado Springs, CO 80933 ATTN: Dr. Michael J. Normandia
1	Cercom, 1950 Watson Way, Vista, CA 92083 ATTN: Rich Palicka
1	Poulter Laboratory, SRI International, 333 Ravenswood Avenue, Menlo Park, CA 94025 ATTN: Dr. Donald Curran
1	Dr. Lynn Seaman
1	Dr. Donald A. Shockey
1	Dr. Robert D. Caligiuri

No. of Copies	To
1	Alliant Techsystems, Inc., 7225 Northland Drive, Brooklyn Park, MN 55428-1515
1	ATTN: T. J. Holmquist
1	Dr. Gordon R. Johnson
1	E. I. Du Pont de Nemours & Company, Wilmington, DE 19898
1	ATTN: Dr. Barry E. Bowen
1	California Research & Technology, Inc., 5771 Johnson Drive, Pleasanton, CA 94566
1	ATTN: Dr. Ronald E. Brown
1	Aeronautical Research Associates of Princeton, Inc., 50 Washington Road, P.O. Box 2229, Princeton, NJ 08540
1	ATTN: Dr. Ross M. Contiliano
1	Dow Chemical Company, Midland, MI 48640
1	ATTN: Mr. Kenneth O. Groves
2	Director, U.S. Army Research Laboratory, Watertown, MA 02172-0001
5	ATTN: AMSRL-OP-CI-D, Technical Library
	Author